Synthesis, DFT calculations, spectroscopic and photovoltaic of the novel N″, N‴-*bis*[(4,9-dimethoxy-5-oxo-5*H*-furo[3,2-*g*]chromen-6-yl) methylidene] thiocarbonohydrazide (**BFCMT**) and its photodiode application

A.A.M. Farag [a, b, *], Magdy A. Ibrahim [c], Shimaa Abdel Halim [c], N. Roushdy [d], Nasser M. El-Gohary [c]

[a] *Physics Department, Faculty of Science and Arts, Aljouf University, Saudi Arabia*
[b] *Thin Film Laboratory, Physics Department, Faculty of Education, Ain Shams University, Roxy, 11757, Cairo, Egypt*
[c] *Department of Chemistry, Faculty of Education, Ain Shams University, Roxy, 11757, Cairo, Egypt*
[d] *Electronics Materials Dep. Advanced Technology& New Materials Research Inst., City of Scientific Research & Technological Applications (SRTA-City), New Borg El-Arab City, P.O. Box: 21934, Alexandria, Egypt*

ABSTRACT

Condensation reaction of 6-formylkhellin (**1**) with thiocarbohydrazide in 2:1 M ratio afforded the novel N″, N‴-*bis* [(4, 9-dimethoxy-5-oxo-5*H*-furo [3,2-*g*]chromen-6-yl) methylidene]thiocarbonohydrazide (**BFCMT**) and its electronic absorption spectrum was interpreted by TD-DFT calculations. The electronic transition is direct allowed with onset and fundamental energy gaps of 1.06 and 3.36 eV, respectively. The estimated optical constants were applied to evaluate the optical transition type as well as the effective optical parameters. The current density-voltage characteristics of **BFCMT**/p-Si heterojunction at 300 K in dark and under illumination of 100 mW/cm^2 showed rectifying characteristics. The capacitance-voltage characteristic parameters under illumination showed a reduction in the built-in potential and increasing the active carrier concentration. The loaded J—V characteristics of **BFCMT**/p-Si heterojunction under illumination were investigated and showed a remarkable power conversion efficiency of 0.83% without consideration of the refection correction or losses from the upper electrode absorption.

© 2017 Elsevier B.V. All rights reserved.

1. Introduction

The regular furochromone khellin (4,9-dimethoxy-7-methyl-5-oxo-5H-furo[3,2-g] chromene) acquired from the products of the soil of Ammi visnaga L is a notable medicinal substance [1–4]. Khellin has gotten extensive consideration to a great extent on account of its vasodilatory properties and of its capacity to instigate skin pigmentation upon ultraviolet light treatment of patient experiencing vitiligo [5]. Khellin have occupied a position of considerable importance due to their widespread occurrence in the plants and their potential use as pharmaceuticals [6—10]. DFT-theoretical calculation can be investigate the optimized geometries of the synthesized compound N″, N‴-*bis*[(4,9-dimethoxy-5-

oxo-5*H*-furo[3,2-*g*]chromen-6-yl)methylidene]thiocarbonohy-drazide (**BFCMT**), see Scheme 1. Furthermore, to examine the impact of dissolvable extremity on the visible spectra and consequently, anticipating the relative dependable qualities, the degree of charge exchange character and task of the watched electronic changes groups as limited, delocalized or potentially of charge exchange (CT) has been encouraged by TD-DFT calculation [11]. In this work, our team work make an attempt to synthesize symmetrical thiocarbohydrazone bearing two khellin moieties in one molecular frame of photoluminescence. The analysis of the absorption edge of the films is also investigated to determine the optical energy gap which is significant for solar cell application. The current-voltage and capacitance voltage characteristics in dark and under 100 mW/cm^2 are employed to extract the main important parameters and examine the appropriate condition for the studied heterojunction in the scope of photovoltaic device application.

* Corresponding author. Thin Film Laboratory, Physics Department, Faculty of Education, Ain Shams University, Roxy, 11757 Cairo, Egypt
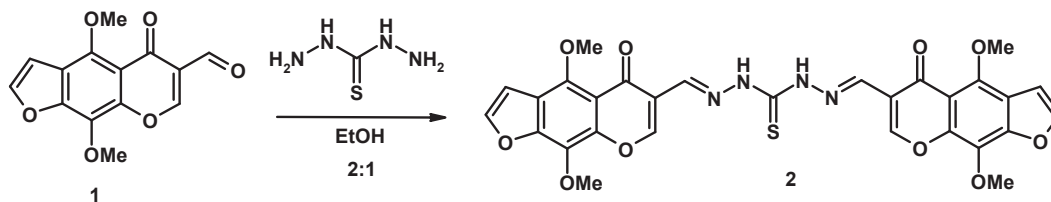
Scheme 1.

2. Experimental

2.1. Preparation and molecular structural characterizations of BFCMT

A solution of hot carboxaldehyde **1** (0.55 g, 2 mmol) was compile in absolute ethanol (20 mL), thiocarbohydrazide (0.11 g, 1 mmol) and the blend was warmed under reflux for 10 min. The yellow crystals obtained during heating were filtered off and crystallized from ethanol to give **BFCMT** as yellow crystals. Yield (0.34 g, 55%), m.p. 205–206 °C. IR (KBr, cm^{-1}): 3269 (NH), 3207 (CH$_{furan}$), 3064 (CH$_{arom}$), 2993, 2950 (CH$_{aliph}$), 1644 (C=O$_{\gamma\text{-pyrone}}$), 1620 (C=N), 1550 (C=C), 1219 (C=S). ^{1}H NMR (300 MHz, DMSO-d_6): 3.99 (s, 3H, OCH$_3$), 4.12 (s, 3H, OCH$_3$), 7.29 (d, 1H, J = 1.8 Hz, H-3$_{furan}$), 7.91 (d, 1H, J = 1.8 Hz, H-2$_{furan}$), 8.23 (s, 2 H, CH=N), 9.18 (s, 2 H, H-7), 10.39 (s, 2 H, 2NH exchangeable with D$_2$O). Mass spectrum, m/z (I_r %): 618 (M$^+$, 2), 598 (2), 543 (2), 509 (3), 404 (15), 288 (22), 272 (17), 257 (11), 242 (34), 220 (86), 205 (100), 191 (30), 177 (93), 163 (31), 147 (21), 134 (13), 119 (29), 95 (99), 77 (54), 66 (79). Anal. Calcd for C$_{29}$H$_{22}$N$_4$O$_{10}$S (618.57): C, 56.31; H, 3.58; N, 9.06; S, 5.18%. Found: C, 56.25; H, 3.40; N, 8.85; S, 5.01%.

The detailed specifications for all the physical measurements were reported by the team workers in the literature [12–14].

2.2. Computational method

All the calculations in the presented manuscript were achieved utilizing DFT method subjected to B3LYP method [11]. This function was full previously discussed in the literature by Lee et al. [15]. Moreover, the optimization for the structure geometry was achieved with helping of the 6-311G (p,d) bases set [16] as performed by Gaussian 09 package [17].

2.3. Thin film preparation and physical characterizations of BFCMT

For the **BFCMT** thin film preparation, a thermal evaporation technique type 306 A was used. The cleaning procedure of the corning glasses and Si substrates and the formation of the front and back ohmic contacts have been defined by the same procedure of our previous studies [17]. The surface morphology of **BFCMT** were obtained by scanning electron microscopy, type JEOL-JSM-636 OLA (SEM). A normal transmission and reflectance measurement were realized by JASCO-670 UV/VIS/NIR spectrophotometer. The dark and illuminated (100 mW/cm^2) current-voltage characteristics of the heterojunction were measured by Keithly 2635 A through a full computerized system.

3. Results and discussion

3.1. Molecular structure and reaction confirmation

In the present work, condensation reaction of 6-formylkhellin (4,9-dimethoxy-5-oxo-5H-furo[3,2-g]chromen-6-

carboxaldehyde) (**1**) with thiocarbohydrazide in 2:1 M ratio afforded the novel N″,N‴-bis[(4,9-dimethoxy-5-oxo-5H-furo[3,2-g] chromen-6-yl)methylidene]thiocarbonohydrazide (**BFCMT**) (Fig. 1a). Structure of **BFCMT** was deduced on the basis of its correct analytical and spectral data. The experimental IR spectrum of the compound was done and summarized in Table 1. The characteristic absorption bands at ν_{max} 3269 (NH), 3207 (CH$_{furan}$), 3064 (CH$_{arom}$), 2993, 2950 (CH$_{aliph}$), 1644 (C=O$_{\gamma\text{-pyrone}}$), 1620 (C=N), 1550 (C=C) and 1219 cm^{-1} (C=S). The ^{1}H NMR spectrum of **BFCMT** revealed the presence of singlet signals at δ 3.99 (OCH$_3$), 4.12 (OCH$_3$), 8.23 (CH=N), 9.18 (H-7), as well as two doublets assigned to H-3$_{furan}$ and H-2$_{furan}$ at δ 7.29 and 7.91, respectively. The spectrum also revealed D$_2$O-exchangeable signal at δ 10.39 attributed to NH protons. Furthermore, structure of **BFCMT** was deduced from its mass spectrum which revealed the molecular ion peak at m/z 618 which agrees well with the suggested molecular formula C$_{29}$H$_{22}$N$_4$O$_{10}$S. FT-IR spectra of **BFCMT**, calculated at B3LYP/6-311G (d,p), are listed in Table 1. Another attempt to follow up the changes of the studied compound **BFCMT** is carried out by studying vibrational spectra. The computed vibration is assigned to C–H aromatic stretching vibrations at 3222 cm^{-1} for **BFCMT** which is comparable
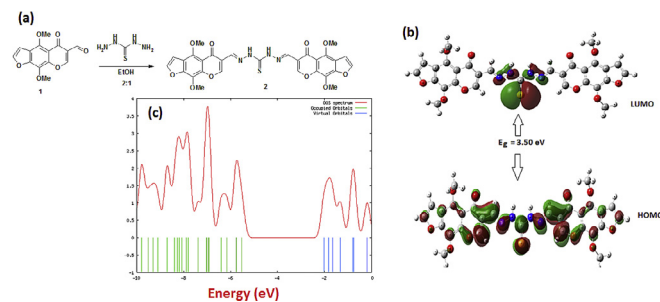

Fig. 1. (a) Formation of the novel **BFCMT**, **(b)** Optimized geometry, numbering system, net charge, vector of dipole moment, HOMO and LUMO using B3LYP/6-311G(d,p), and (c) Density of states (DOS) of **BFCMT**.

Table 1
Experimental and computational calculated vibrational wave-numbers (harmonic frequency (cm^{-1})), IR intensities and assignments for compound **BFCMT** at the B3LYP/6-311G (d,p).

No.	$\upsilon_{exp.}$(cm^{-1})	$\upsilon_{the.}$(cm^{-1})	Intensity	Assignment
1	3269	3451	49.36	N-H Twisting
2	3207	3260	2.27	C-H furan Asym Stretching
3	3064	3222	0.48	C-H aromatic Asym Stretching
4	2993, 2950	3017, 3024	76.23, 58.69	C-H aliphatic Sym Stretching
5	1644	1699	252.79	C=O γ-pyrone Asym Stretching
6	1620	1677	0.25	C=N Asym
7	1550	1583	14.22	C=C (in ring)
8	1219	1325	8.87	C=S Twisting

with experimental results at 3064 cm^{-1} [18]. The computed vibration is assigned to symmetric C—H aliphatic stretching vibration in CH$_3$ at 3017 and 3024 cm^{-1} respectively for **BFCMT** has shown a comparable agreement with those for experimental at 2993 and 2950 cm^{-1}, respectively. The computed vibration is assigned to asymmetric C—H furan stretching vibration at 3260 cm^{-1} which has shown a comparable agreement with experimental results at 3207 cm^{-1}. The computed vibration is assigned to N—H twisting vibration at 3451 cm^{-1} which has shown a comparable agreement with experimental results at 3269 cm^{-1}. Generally the C═O vibrations [19] is observed in the region 1790–1810 cm^{-1}. Vibrations is assigned to C═O stretching at 1699 cm^{-1} which is comparable with experimental results at 1644 cm^{-1}. The computed vibration at 1583 cm^{-1} is assigned to C═C stretching vibrations [20,21] which matches with those experimental at 1550 cm^{-1}. Moreover, the computed and experimental vibrations at 1677 cm^{-1} and 1620 cm^{-1}, respectively are assigned to the asymmetric C═N stretching vibration. The computed vibration is assigned to C═S stretching vibration at 1325 cm^{-1} has shown a comparable agreement with experimental results at 1219 cm^{-1}.

Table 2
Optimized calculations of total energies (a.u.), zero point vibrational energies (kcal.mol^{-1}), rotational constants (GHz), entropies (cal.k^{-1}), energy of HOMO and LUMO (eV), energy gap (eV) and total dipole moment (Debye) for N″,N‴-bis[(4,9-dimethoxy-5-oxo-5H-furo[3,2-g]chromen-6-yl)methylidene]thiocarbonohydrazide (**BFCMT**) at the B3LYP/6-311G(d,p).

Parameters	B3LYP/6-311G
Total Energy,(E$_T$)	−2488.11866923
Zero Point Vibrational Energy	300.44659
	0.24272
Rotational constant	0.01433
	0.01367
Entropy	
Total	255.556
Translational	45.148
Rotational	40.043
Vibrational	170.365
Energy of highest occupied molecular orbital (E$_{HOMO}$)	5.526224
Energy of lowest unoccupied molecular orbital (E$_{LUMO}$)	2.023136
Energy Gap,(E$_g$)	3.503088
Dipole moment, (μ)	1.9141

3.2. Molecular orbital calculations

The optimized geometries and the ground state energies of **BFCMT**, were extracted by using the B3LYB/6-311G (p,d) level and listed in Table 2 and Fig. 1(b). The total energies and the change in the total entropy of **BFCMT** at 300 K using B3LYP/6-311G (d,p) are also calculated. The analysis of Table 2 shows that the optimized bond length of C═C in phenyl ring falls in the range from 1.357 to 1.472 Å which is in harmony with those experimental data of 1.481 Å [20]), for C═O bonds the optimized length obtained by B3LYB/6-311G (p,d) is slightly shorter than the experimental data 1.229 Å [20]. The computed bond angles are largely affected by the presence of C═O group in C4, especially < H$_{44}$C$_{43}$O$_{45}$, <N$_{35}$N$_{36}$C$_{30}$ and <C$_{40}$C$_{41}$O$_{46}$ are 123.56°, 117.19° and 123.97° respectively. The highly stable geometry of **BFCMT** is the planar structure, except methoxy moiety (where the dihedral angle is between 0.00° and 180°). The ionization energy, I.E, of compound **BFCMT** is 5.53 eV (Table 2). Also, the electron affinity (E.A) of **BFCMT** is 2.02 eV. So the calculated E_g of **BFCMT** is 3.50 eV. Finally, the computed dipole moment (μ) of **BFCMT** is found to be 1.91 D. In addition, the zero point vibrational energy and the total entropy are found to be 400.44(kcal.mol^{-1}) and 255.556 cal k^{-1}, respectively (Table 2).

3.3. Density of states calculation (DOS)

The HOMO−LUMO energy gaps are reduced under the influence of **BFCMT** and shown in Table 2 and Fig. 1(b). The clarification of the distinctions in photo-to-current conversion efficiency because of BFCMT is looked for in the DOS system demonstrates the number of states per energy interval at each energy level, which is accessible to be possessed by electrons. A high DOS at a particular energy level implies that there are many states accessible for occupation, and subsequently scales straightly with the photovoltaic conversion effectiveness. In Fig. 1(c), the calculated DOS of the **BFCMT** is presented to clarify the effect of **BFCMT**. As shown, the DOS becomes more abundant near Fermi levels; so reflecting the predominant effect of **BFCMT** on enhancing the cell performance.

3.4. Electronic absorption spectra of BFCMT

The electronic spectra of compound **BFCMT** in acetone and xylene solvents, assignment of spectra are given in Table 3. The

Table 3
Calculated band maxima and intensities of compound **BFCMT** by TD method.

State	Theoretical					Experimental	
	Configuration	Coefficient	λ, nm	f	Type	Polar λ, nm	Non polar λ, nm
I	158−162	0.16131	377.32	1.1071	$\pi - \pi^*$	370.84	383.53
	159−161	0.66112			$\pi - \pi^*$		
II	156−161	0.10598	337.92	0.3936	$\pi - \pi^*$	331.94	343.98
	157−162	−0.24390			$\pi - \pi^*$		
	158−162	−0.17323			$\pi - \pi^*$		
	158−164	−0.21134			$\pi - \pi^*$		
	159−163	0.52735			$\pi - \pi^*$		
	160−164	−0.17029			$\pi - \pi^*$		
					$\pi - \pi^*$		
III	156−161	0.52002	307.17	0.3532	$\pi - \pi^*$	302.73	315.78
	156−163	−0.14854			$\pi - \pi^*$		
	157−162	0.35600			$\pi - \pi^*$		
	158−164	−0.19499			$\pi - \pi^*$		
					$\pi - \pi^*$		
					$\pi - \pi^*$		
					$\pi - \pi^*$		

spectrum in xylene is composed of three bands centered at 383.53 nm, 343.98 nm and 315.78 nm. Increasing solvent polarity on going from xylene to acetone causes small changes in band positions indicating that the polarity of the excited and ground state are of the same values, that is, solvent independent. The band in the range of 4000–24000 with lower intensity are assigned to π-π* of acetone. The excited configurations considered in **BFCMT** are those which results from an electron excitation of five highest occupied molecular orbital's and the lowest four unoccupied molecular orbital's. The matching between the theoretically and experimentally results are satisfactory.

The first $(\pi\text{-}\pi^*)^1$ state is centered at 383.53 nm in xylene this band is predicted theoretically at 377.32 nm, in matching with the experiment. This band is of CT character from bis (furochromen) moiety to the thiocarbonohydrazide moiety. The second $(\pi\text{-}\pi^*)^1$ state is observed at 343.98 nm in xylene and is predicted theoretically at 337.92 nm. This band is composed of six configurations. This band has CT character from *bis* (furochromen) moiety to the thiocarbonohydrazide moiety, delocalized and localized bands. The third $(\pi\text{-}\pi^*)^1$ state is observed in xylene at 315.78 nm and predicted theoretically at 307.17 nm and consists of a mixture of four configurations, (c.f. Table 3), that is, CT, localized and delocalized configurations may be expected. The main contribution of this band is coming from the two configurations, which is of CT character from bis(furo-chromen) moiety to the thiocarbonohydrazide moiety and delocalized.

3.5. Surface morphology characterization

Fig. 2(a–c) shows various images of **BFCMT** obtained by scanning electron microscopy (SEM), alternating the same magnification order (on the scale of 5 μm, ×5,000) from various situations to check the analogy. Particle size analyzer instrument was used for estimating the average value of the particle size which is found to be about 370 nm, Fig. 2(d). The same feature of all the images is the high agglomerations of the particles without defined structure. These type of agglomerations may be attributed to the fact that the nature of constituent nanoparticles have not enough homogeneously nature. In addition, there are not any chosen orientations for the nanoparticles, indicating random nanoparticles orientations. This behavior was confirmed by using X-ray diffraction analysis, shown in Fig. 2(e), which indicates an amorphous nature for the **BFCMT** samples.
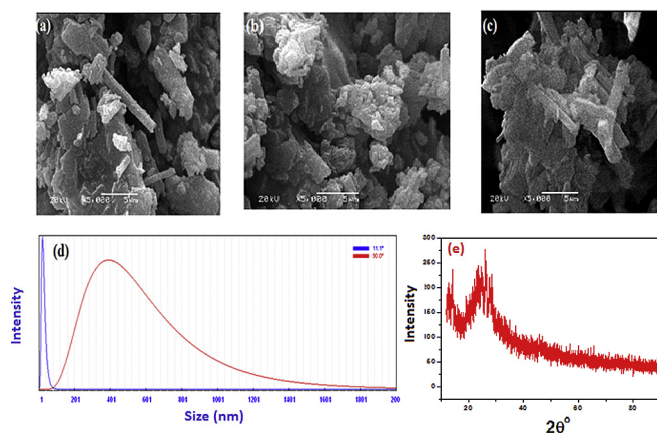

Fig. 2. (a–c) SEM of different magnifications (a)1000×, (b) 5,000, (c) 10,000, (d) particle size analysis, and (e) X-ray diffraction of **BFCMT** thin film.

3.6. Optical characterizations of BFCMT thin films

A wide wavelength dependence of both transmittance T (λ) and reflectance R (λ) is demonstrated in Fig. 3(a). A small interference fringes is shown for T in the transparent region, followed by a high intensity approaching to 89%. At lower wavelength the absorption begins to exist, the intensity of the transmission starts to decrease and approaches the strong absorption region correlated with the material band edge. The significant optical constants namely refractive index, n and absorption index, k of **BFCMT** film were calculated within accuracy of ±4% for n and ±3% for k.

The dispersion, n and absorption index, k behaviors of **BFCMT** film in the wavelength range of 200–2500 nm (not shown here). As observed, the Figure mentions that anomalous dispersion at shorter wavelength followed by a normal dispersion at longer wavelength. The results show a sharp peak centered at 370 nm, which can be due to the fundamental energy gap in the UV region. At wavelength of 675 nm, k vanishes, after which it begins to increase with increasing wavelength, which is a characteristic feature of existence of free carrier absorption [22]. The energy gaps, E_g, and the electronic transition type of **BFCMT** film were calculated from the analysis of the absorption coefficient, α near the optical absorption edge using the relationship [13]

$$(\alpha h\nu) = C(h\nu - E_g)^s \tag{1}$$

where C is a constant and the exponent, s relates to the type of transition, where s = 2 or 3 for indirect allowed and forbidden transitions, respectively and s = 1/2 or 3/2 for direct allowed and forbidden transitions, respectively. Fig. 3(b)and (c) illustrate the plots of $(\alpha h\nu)^2$ against hν for BFCMT thin films. The optical band gap energy for allowed direct transition is estimated by the extrapolation of linear part to $(\alpha h\nu)^2 = 0$. The values of energy gaps were found to be 1.06 and 3.36 eV. Any confliction amongst the calculated and experimental values might be because of the way that the calculations have been really performed [13,14].

3.7. Dispersion characteristics

For the higher wavelengths, where λ > 800 nm, the refractive index shows a normal dispersion which can be explained under consideration of the single oscillator model. The single oscillator parameters can be obtained by using the expression suggested by Wemple and Di-Domenico as follows [23]:

$$\left(n^2 - 1\right)^{-1} = \frac{E_0}{E_d} - \frac{1}{E_0 E_d}(h\nu)^2 \tag{2}$$

where E_o is known as the oscillator energy and E_d is known as the dispersion energy. The Wemple- Di-Domenico plot (i.e. $(n^2-1)^{-1}$ against E^2) is demonstrated in Fig. 4 (a). The values of E_0 and E_d can easily be calculated and found to be 3.9 and 12.19 eV, respectively.
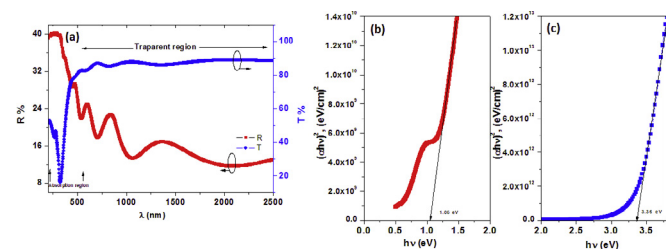

Fig. 3. (a) Spectral dependence of T and R characteristics, (b) Plot of $(\alpha h\nu)^2$ vs. hν of region I and (c) region II of **BFCMT** thin films.
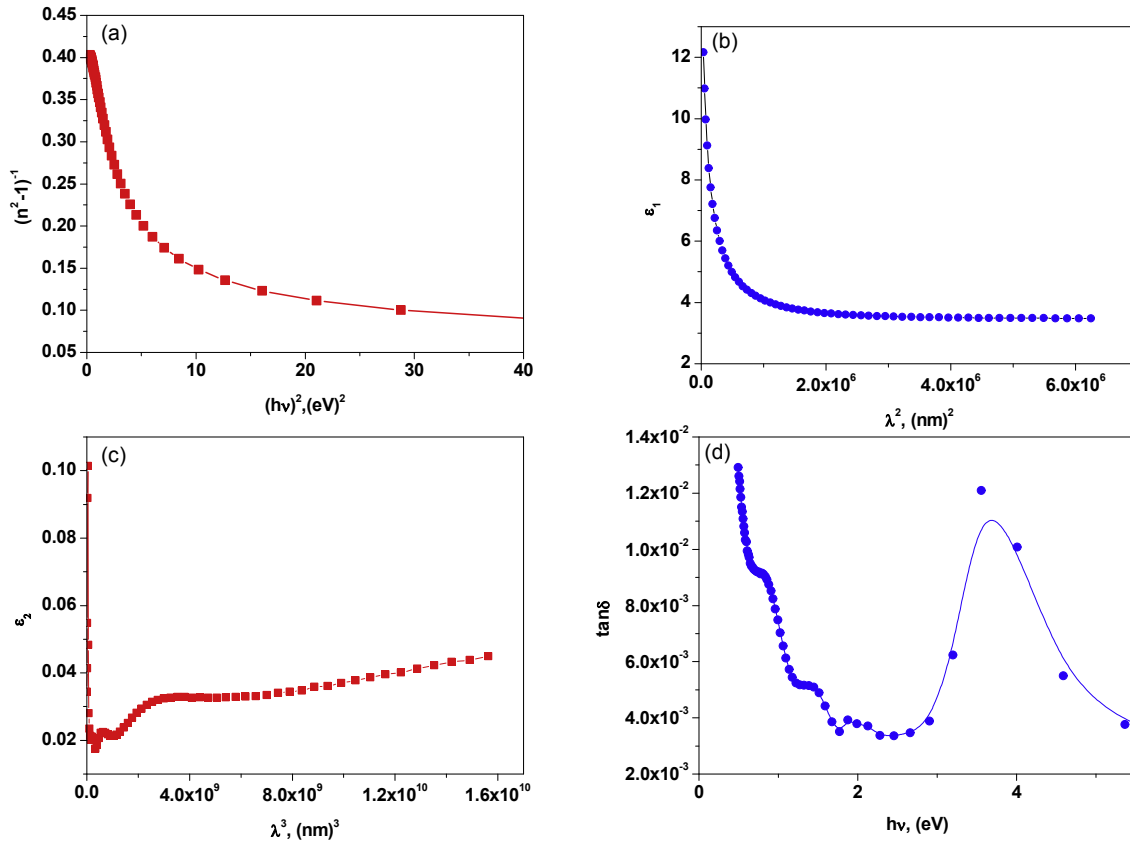
Fig. 4. (a) Plot of $(n^2-1)^{-1}$ vs. $(h\nu)^2$, (b) Plot of ε_1 vs. λ^2, (c) Plot of ε_2 vs. λ^2 and (d) plot of $\tan\delta$ vs. $h\nu$ for **BFCMT** thin films.

The spectral distribution of both the real dielectric constant, ε_1, and imaginary dielectric constant, ε_2 against λ^2 in the transparent region is illustrated in Fig. 4 (b) and (c). As observed, ε_1 decreases with increasing λ^2, while ε_2 increases. In all cases, for higher λ^2, the dependence of both ε_1 on λ^2 has a linear fit. Accordingly, the value of the high frequency dielectric constant, $\varepsilon\infty$ is obtained by extrapolating the straight segment of the curve to the intersection with the ordinate axis. The value of $\varepsilon\infty$ is found to be 3.85 which is in comparable with those for most organic semiconductors [24].

The photon energy dependence for the loss tangent function for the BFCMT thin films is shown in Fig. 4 (d). This figure shows many distinct peaks with different intensities and the peak at nearly 3.6 eV is corresponding to E_g as obtained above.

3.8. Current density–voltage characteristics

The current density-voltage characteristics of **BFCMT**/p-Si heterojunction in dark and under illumination of 100 mW/cm^2 are shown in Fig. 5(a). As observed from the Figure, the prepared heterojunction is characterized by a desirable rectifying characteristic. Moreover, when the heterojunction is illuminated by 100 mW/cm^2, an additional free charge carriers generated in the heterojunction which carriers increase the reverse biased current when contrasted with the forward one [25]. To give information about the predominant conduction mechanism for the forward biased current, the current density-voltage characteristics plot of Fig. 5 (a) is re-plotted as a double logarithmic representation and given in Fig. 5(b) and (c). As observed, each curve has two distinct linear parts with different slopes that complies relation of $J\,\alpha V^m$ (m is the exponent). These two linear parts have different slopes that obey $J\,\alpha V^m$ (m is the exponent) relation. The values of m are found
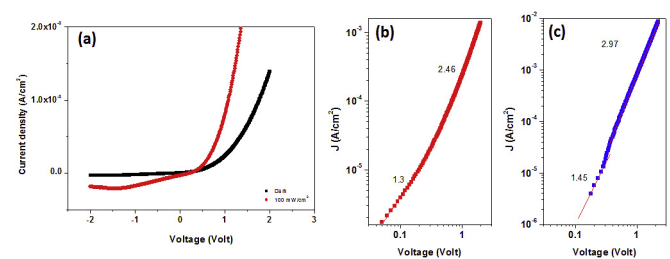

Fig. 5. (a)Plot of current density vs. V in dark and under illumination of 100 mW/cm^2, (b) Plot of logarithmic J vs. V in dark and (c) Plot of logarithmic J vs. V under illumination of 100 mW/cm^2 for **BFCMT**/p-Si heterojunction.

to be 1.3, 2.46 for the characteristics under dark condition and 1.45, 2.97 under illumination for the low and high bias, respectively. In the lower voltage region, the predominant conduction mechanism shows an ohmic behavior, while the behaviors undergo the space-charge-limited-current mechanism under high voltage bias. This behavior is in agreement with those published by various authors for different organic –based devices [26–28].

It is well-known that the series resistance (R_S) is a very significant parameter that has an impact on the electrical characteristics of the device. Therefore, The Cheung and Cheung [29] relationship can be applied for the downward curvature region of the *J-V* characteristics according to the following Equation

$$\frac{dV}{d(\ln J)} = JR_s + \eta\left(\frac{kT}{q}\right) \tag{3}$$

where η is the ideality factor, R_s is the series resistance, k is the

Boltmann's constant, q is the electronic charge. The relationship of dV/dln(J) versus current in the higher voltage region is analyzed (not shown here). Accordingly, the slope and y-axis intercept of the plot allow determination of both R$_S$ and ideality factor, respectively. The obtained series resistance and ideality factor are found to be 3.04,158 Ω and 4.4 and 38 Ω. As observed, there is a remarkable difference between the values of ideality factors and the series resistance obtained from the heterojunction in-dark and under influence of illumination [30]. This change can be because of the impact of the illumination on the charge transporter of the device [31]. In addition, the higher value of the series resistance and ideality factor in the two cases confirm the probability of the presence of inhomogenities of the barrier or the occurrence of interface states [32]. The responsively (R) of the device can be realized from the device sensitivity for the influence of light and can be obtained from the ratio of the photocurrent to the incident light power ($= \frac{I_{ph}}{P}$) [33].

The relationship of the responsively against incident power of illumination is illustrated in Fig. 6 (a). As observed, the values of responsivity are increase with increasing the incident illumination, in the desired applied range, confirming the probability of the prepared heterojunction for various electronic application [34].

Another important parameter, namely, the photosensitivity, Ps is recognized as the ratio of the photocurrent to the dark one ($= \frac{I_{ph}}{I_d}$). The variance of Ps under the influence of applied voltage is illustrated in Fig. 6 (b). A remarkable decreasing for the photosensitivity with increasing the applied voltage. This behavior can be attributed to the increase for the dark current with applied voltage at the same incident light as compared to the photocurrent. This behavior is in agreement with the results published by Yahia et al. [35].

3.9. Capacitance −voltage characteristics

It is well-known that the capacitance-voltage characteristics of the device are considered a major tool for giving essential properties of the device structures [36]. The dark and illuminated capacitance-voltage characteristics of BFCMT/p-Si heterojunction at high frequency of 1 MHz is shown in Fig. 7(a). As seen from the figure, a remarkable dependence for the measured capacitance on applied bias. Moreover, the C^{-2}-V characteristics, shown in Fig. 7(b), is linearly fit under effect of the two conditions. The depletion capacitance of the heterojunction is expressed by the following equation [33];

$$C^{-2} = \frac{2(V_R + V_b)}{q\varepsilon N_A A^2}$$ (4)

where V_R is the reverse bias, V_b is the built-in potential, N_A is the active carrier concentration and ε is the permittivity of the semiconductor. The value of N_A and V_b can easily be obtained from the slope and the extrapolation of the C^{-2}-V plot to the V-axis, respectively. The obtained values of N_A and V_b are found to be 0.64 V, 4.12 × 10^{13} cm^{-3} and 0.245, 6.3 × 10^{13} cm^{-3} for the condition of dark and illumination (100 mW/cm^2), respectively. As observed, a lower value of the built-in potential and carrier concentration for the heterojunction under illumination as compared to those for in dark. The reduction in the built-in potential and increasing the active carrier concentration under illumination means an enhancement of the heterojunction performance and show best control for optoelectronic application [37].

3.10. Photovoltaic characteristics

The loaded J−V characteristics of BFCMT/p-Si heterojunction under illumination of 100 mW/cm^2 are shown in Fig. 8 (a). The heterojunction demonstrates a short circuit current density (J_{sc}) of 7 × 10^{-7}A and an open-circuit voltage (V_{oc}) of 0.29 V. Fig. 8(b) shows the out-put power versus applied voltage. The out-put power reaches to its extreme at a certain applied voltage. Accordingly, the maximum current (J_{max}) and voltage (V_{max}) can easily be extracted which are found to be 4.9 × 10^{-7} A and 0.17 mV. Consequently, the fill factor can be determined using the following expression [38,39]:

$$FF = \frac{J_{max}V_{max}}{J_{sc}V_{oc}}$$ (5)

and calculated as 0.41. In addition, the power conversion efficiency (η) of solar cell is obtained by the following formula [40,41]:

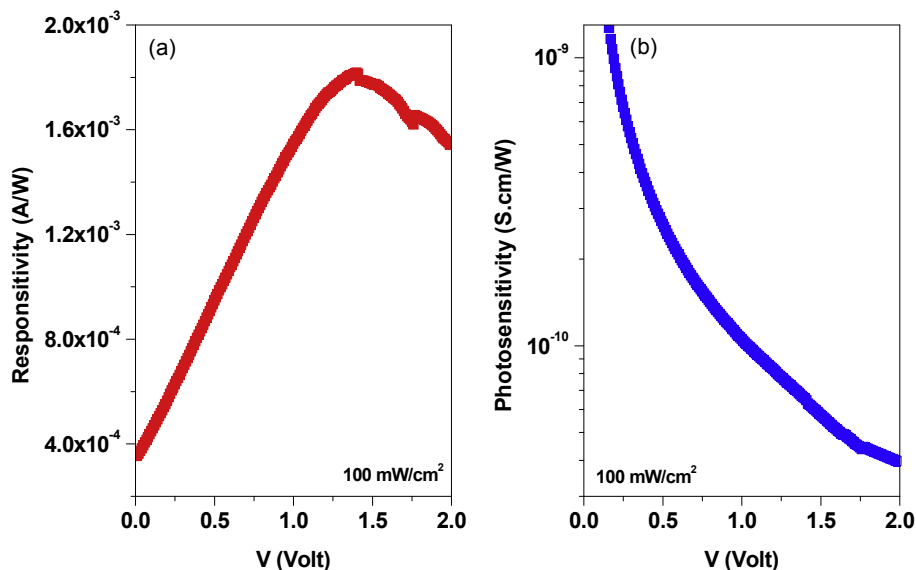$$\eta = \frac{P_{max}FF}{J_{sc}V_{oc}P}x100$$ (6)

Fig. 6. (a) Plot of responsivity vs. V and (b) Plot of photosensitivity vs. V under illumination of 100 mW/cm^2 for **BFCMT**/p-Si heterojunction.
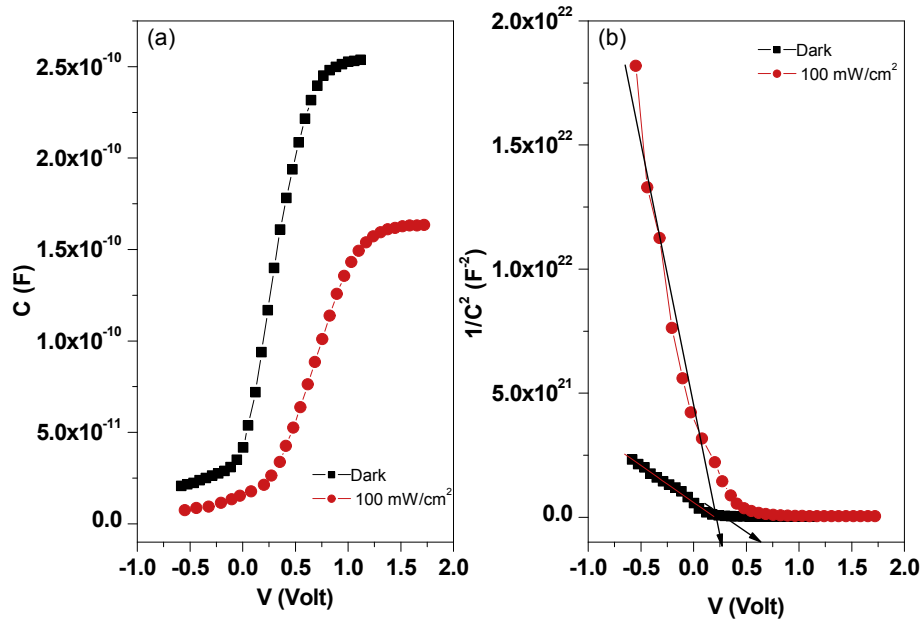
Fig. 7. (a) Plot of C vs. V in dark and under illumination of 100 mW/cm^2 and (b) plot of $1/C^2$ vs. V in dark and under illumination of 100 mW/cm^2 for **BFCMT**/p-Si heterojunction.
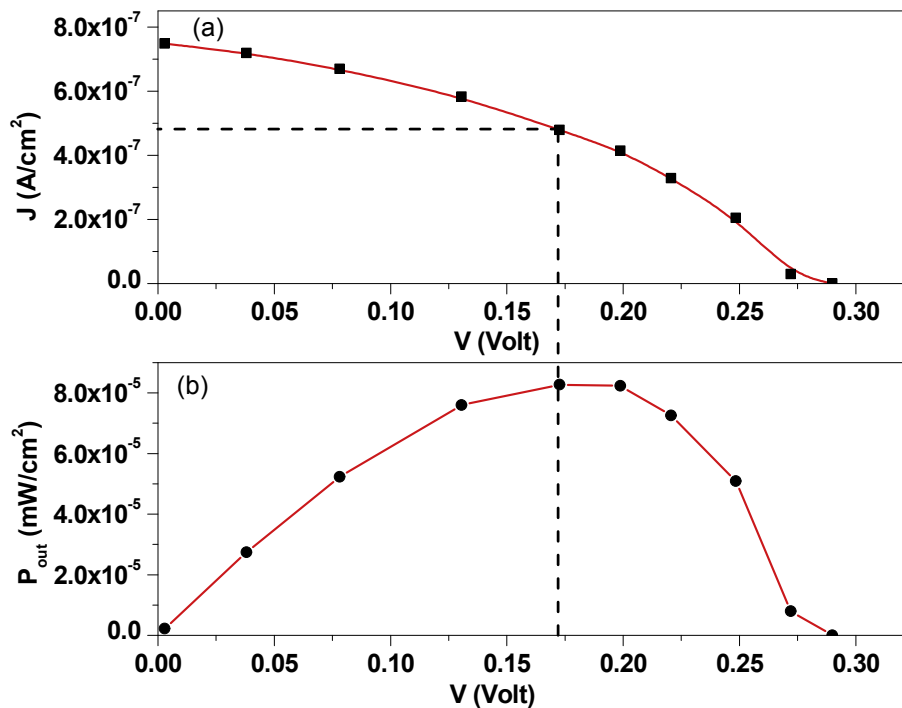

Fig. 8. (a) Plot of J vs. V under illumination of 100 mW/cm^2 and (b) Plot of P_{out} vs. V of **BFCMT**/p-Si heterojunction.

The extracted η value is found to be 0.83%. This value is determined without consideration of the refection correction or losses from the upper electrode absorption. The obtained value of η is comparable with those obtained for various organic based heterojunctions [40,41].

4. Conclusion

The main optical constants of the **BFCMT** thin films in the desired wavelength range of 200–2500 nm using the spectrophotometric measurements. The analysis of the absorption coefficient edges display the presence of two allowed direct optical transitions with energy gaps of 1.06 and 3.36 eV. Based on the single oscillator model and using the Wemple-DiDominco relationship, the single oscillator and dispersion energy were estimated and found to 3.9 and 12.19 eV, respectively. The dark and illuminated current density–voltage and capacitance–voltage characteristics suggest a considerable sensitivity for the effect of illumination of 100 mW/cm^2. In addition, an ohmic followed by the space-charge-limited transport dominate the current in the lower

and higher voltage region, respectively. Under illumination of $100\ mW/cm^2$ light intensity, the maximum current, maximum voltage, power conversion efficiency were extracted and found to be 4.9×10^{-7} A and 0.17 mV and 0.83%, respectively. These values are comparatively comparable with most organic-based photovoltaic devices.

References

[1] M.S. Karawya, M.A. El-Kiey, A. Sina, G. Nour, Simultaneous TLC separation of khellin and visnagin and their assay in *Ammi visnaga* fruits, extracts, and formulations, J. Pharm. Sci. 59 (1970) 1025–1027.

[2] Sneader W. England, Drug Discovery: a History, Wiley Press, 2005.

[3] M.M. El-Domiaty, Improved high-performance liquid chromatographic determination of khellin and visnagin in *Ammi visnaga* fruits and pharmaceutical formulations, J. Pharm. Sci. 81 (1992) 475–478.

[4] A.A. Abu-Hashem, M. El-Shazly, Synthesis, reactions and biological activities of furochromones: a review, Eur. J. Med. Chem. 90 (2015) 633–665.

[5] B. Ortel, A. Tanew, H. Hönigsmann, Treatment of vitiligo with khellin and ultraviolet A, J. Am. Acad. Dermat. 18 (1988) 693–701.

[6] Jihan M. Badr, Ghada M. Hadad, Khaled Nahriry, Hashem A. Hassanean, Validated HPLC method for simultaneous estimation of khellol glucoside, khellin and visnagin in Ammi visnaga L. fruits and pharmaceutical preparations, J. Nat. Prod. Res. 29 (2014) 593–601.

[7] J. Bauer, J.W.T. Selway, J.F. Batchelor, M. Tisdale, I.C. Caldcoell, D.A.B. Young, 4′, 6-Dichloroflavan (BW683C), a new anti-rhinovirus compound, Nature 292 (1981) 396–398.

[8] H. Ishitsuka, C. Ohsawa, T. Ohiwa, I. Umedo, Y. Suhara, Antipicornavirus flavone Ro 09-0179, Antimicrob. Agents Chemother. 22 (1982) 611–616.

[9] R.B. Gammill, C.E. Day, P.E. Schurr, Khellin analogs. 1. General topological requirements for lipid-altering activity in furochromones, J. Med. Chem. 26 (1983) 1672–1674.

[10] P. Vanachayangkul, K. Byer, S. Khan, V. Butterweck, An aqueous extract of *Ammi visnaga* fruits and its constituents khellin and visnagin prevent cell damage caused by oxalate in renal epithelial cells, Phytomedicine 17 (2010) 653–658.

[11] (a) A.D. Becke, Density-functional thermochemistry. III. The role of exact exchange, J. Chem. Phys. 98 (1993) 5648–5652;
(b) A.D. Becke, Density-functional thermochemistry. I. The effect of the exchange-only gradient correction, J. Chem. Phys. 96 (1992) 2155–2160.

[12] Shimaa Abdel Halim, Magdy A. Ibrahim, Synthesis, DFT calculations, electronic structure, electronic absorption spectra, natural bond orbital (NBO) and nonlinear optical (NLO) analysis of the novel 5-methyl-8*H*-benzo[*h*]chromeno [2,3-*b*][1,6] naphthyridine-6(5*H*),8-dione (MBCND), J. Mol. Struct. 1130 (2017) 543–558.

[13] Walid M.I. Hassan, Hussein Moustafa, Mohamed N.H. Hamed, Laila I. Ali, Shimaa Abdel Halim, DFT calculations and electronic absorption spectra of some, α- and γ-pyrone derivatives, Spectrochim. Acta Part A 117 (2014) 587–597.

[14] Hoda F. El-Shafiy, M. Saif, Mahmoud M. Mashaly, Shimaa Abdel Halim, R. Fouad, New nano-complexes of Zn(II), Cu(II), Ni(II) and Co(II) ions; spectroscopy, thermal, structural analysis, DFT calculations and antimicrobial activity application, J. Mol. Struct. 1147 (2017) 452–461.

[15] (a) C. Lee, W. Yang, R.G. Parr, Development of the Colle-Salvetti correlation-energy formula into a functional of the electron density, Phys. Rev. B Condens. Matter 37 (1988) 785–789;
(b) B. Miehlich, A. Savin, H. Stolt, H. Preuss, Results obtained with the correlation energy density functionals of becke and Lee, Yang and Parr, Chem. Phys. Lett. 157 (1989) 200–206.

[16] B. B. Stefanov, G. Liu, A. Liashenko, P. Piskorz, I. Komaromi, R. L. Martin, D. J. Fox, T. Keith, M. A. Al-Laham, C. Y. Peng, A. Nanayakkara, M. Challacombe, P. M. W. Gill, B. Johnson, W. Chen, M. W. Wong, C. Gonzalez, J. A. Pople, Gaussian, Inc., Pittsburgh PA, 2003.

[17] M. J. Frisch, G. W. Trucks, H. B. Schlegel, G. E. Scuseria, et al., Gaussian, Inc., Wallingford CT, 2009.

[18] J.B. Lambert, H.F. Shurvell, L. Vereit, R.G. Cooks, G.H. Stout, Organic Structural Analysis, Academic Press, New York, 1976.

[19] P.S. Kalsi, Spectroscopy of Organic Compounds, Academic Press, New York, 2002.

[20] J.N. Macoonald, S.A. Mackay, J.K. Tyler, A.P. Cox, I.C. Ewart, Synthesis, DFT calculations, electronic structure, electronic absorption spectra, natural bond orbital (NBO) and nonlinear optical (NLO) analysis of the novel 5-methyl-8*H*-benzo[*h*]chromeno[2,3-*b*][1,6] naphthyridine-6(5*H*),8-dione (MBCND), J. Chem. Soc. Farady Trans. II 77 (1981) 79–89.

[21] J.B. Lambert, H.F. Shurvell, L. Vereit, R.G. Cooks, G.H. Stout, Organic Structural Analysis, Academic Press, New York, 1976.

[22] H.M. Zeyada, M.M. El-Nahass, I.S. Elashmawi, A.A. Habashi, Annealing temperatures induced optical constant variations of methyl violet 2B thin films manufactured by the spin coating technique, J. Non-Cryst. Solid 358 (2012) 625–636.

[23] S.H. Wemple, M. DiDomenico, Behavior of the electronic dielectric constant in covalent and ionic materials, Phys. Rev. B 3 (1971) 1338–1351.

[24] A.A.M. Farag, I.S. Yahia, S. Alfaify, A. Bilgicli, M. Kandaz, F. Yakuphanoglu, Optical dispersion parameters based on single-oscillator model and optical absorption of nanocrystalline metal phthalocyanine films: a comparison study, Superlattices Microstruct. 60 (2013) 83–100.

[25] A.S. Dahlan, A.A. Al-Ghamdi, A.A. Al-Ghamdi, S. Bin-Omran, Y. Al-Turki, F. El-Tantawy, F. Yakuphanoglu, Photodiode and photocapacitor properties of Au/CdTe/p-Si/Al device, J. Alloys Compd. 646 (2015) 1151–1156.

[26] R.K. Gupta, F. Yakuphanoglu, H. Hasar, Abdulaziz A. Al-Khedhairy, *p*-Si/DNA photoconductive diode for optical sensor applications, Synth. Met. 161 (2011) 2011–2016.

[27] S. Demirezen, S. Altındal, I. Uslu, Two diodes model and illumination effect on the forward and reverse bias *I–V* and *C–V* characteristics of Au/PVA (Bi-doped)/n-Si photodiode at room temperature, Curr. Appl. Phys. 13 (2013) 53–59.

[28] S. Okur, F. Yakuphanoglu, M. Ozsoz, P.K. Kadayifcilar, Electrical and interface properties of Au/DNA/*n*-Si organic-on-inorganic structures, Microelectron. Eng. 86 (2009) 2305–2311.

[29] M.A. Ibrahim, A.A.M. Farag, N. Roushdy, N.M. El-Gohary, Synthesis, optical and photoelectrical characterizations of the novel 10-chloro-6*H*,8*H*- dichromeno [2,3-*b*:3′,4′-*e*]pyridine-6,8-dione (CDPD) and its photodiode application, Opt. Mater. 51 (2016) 70–77.

[30] S. Karatas, M.G. Aydin, H. Ozerli, J. Alloys Compd. 689 (2016) 1068–1075.

[31] L.C. Chen, M.I. Lu, Effects of spin-polarized injection and photo-ionization of MnZnO film on GaN-based light-emitting diodes, Scr. Matter 61 (2009) 781–784.

[32] J.M. Bluet, D. Ziane, G. Guillot, D. Tournier, P. Brosselard, J. Montserrat, P. Godignon, Barrier height homogeneity for 4.5 kV 4H-SiC Schottky diodes, Superlattices Microstruct. 40 (2006) 399–404.

[33] S.M. Sze, Physics of Semiconductor Devices, Physics and Technology, second ed., Wiley, New York, 2001.

[34] M. Soylu, R. Ocaya, H. Tuncer, A.A. Al-Ghamdi, A. Dere, D.C. Sari, F. Yakuphanoglu, Analysis of photovoltaic behavior of Si-based junctions containing novel graphene oxide/nickel(II) phthalocyanine composite films, Microelectron. Eng. 154 (2016) 53–61.

[35] I.S. Yahia, F. Yakuphanoglu, S. Chusnutdinow, T. Wojtowicz, G. Karczewski, Photovoltaic characterization of n-CdTe/p-CdMnTe/GaAs diluted magnetic diode, Curr. Appl. Phys. 13 (2013) 537–543.

[36] S. Karatas, M.G. Aydin, H. Ozerli, Illumination impact on electrical properties of Ag/0.6 wt% nanographene oxide doped poly(vinyl alcohol) nanocomposite/ p-Si heterojunction, J. Alloys Compd. 689 (2016) 1068–1075.

[37] P. Jain, B.K. Mishra, C-V investigation in optically illuminated MOSFET, Int. J. Eng. Res. Appl. 2 (2012) 1282–1288.

[38] M.M. El-Nahass, H.S. Metwally, H.E.A. El-Sayed, A.M. Hassanien, Electrical and photovoltaic properties of FeTPPCl/p-Si heterojunction, Synth. Met. 161 (2011) 2253–2259.

[39] H.M. Zeyada, M.M. El-Nahass, E.M. El-Menyawy, Fabrication and transport mechanisms of 2-(2, 3-dihydro-1, 5-dimethyl-3-oxo-2-phenyl-1H-pyrazol-4-ylimino)- 2-(4-nitrophenyl) acetonitrile/p-silicon hybrid solar cell, Sol. Energy Mater. Sol. Cells 92 (2008) 1586–1592.

[40] I.M. Soliman, M.M. El-Nahass, B.A. Khalifa, Characterization and photovoltaic performance of organic device based on AlPcCl/p-Si heterojunction, Synth. Met. 209 (2015) 55–59.

[41] H.M. Zeyada, A.A. Habashi, M.M. Makhlouf, A.S. Behairy, M.A. Nasher, Fabrication, electrical transport mechanisms and photovoltaic properties of methyl violet 2B/n-Si hybrid organic/inorganic solar cell, Microelectron. Eng. 163 (2016) 134–139.